Dissociative electron attachment to vibrationally excited CO_2

Hao Li, Xiao-Fei Gao, Xin Meng, and Shan Xi Tian*

Hefei National Laboratory for Physical Sciences at the Microscale, iChEM (Collaborative Innovation Center of Chemistry for Energy Materials), Department of Chemical Physics, University of Science and Technology of China, Hefei 230026, China

(Received 15 January 2019; published 11 March 2019)

Dissociative electron attachment to molecules in vibrationally excited states is associated with lower threshold energies and higher cross sections than for cold targets. To date, fewer studies have been performed for polyatomic molecules than for diatomic molecules, due to the experimental challenges and theoretical difficulties in describing the complicated dynamics. Here we report an observation of the dissociative electron attachment to CO_2 in the vibrationally excited states, where the vibrationally excited CO_2 targets are prepared by the electron-impact excitation at energies close to the $^2\Pi_u$ resonant state of CO_2^-. The high-resolution anion momentum images of the O^- yield indicate that the rovibrational state distributions of the coproduct CO are dependent on the vibrationally excited states of symmetric bond stretching and bending modes of CO_2.

DOI: 10.1103/PhysRevA.99.032703

I. INTRODUCTION

Molecular vibrations have profound effects on chemical reactions [1–3] and physical energy transfers [1,4,5], which arouses a lot of efforts aiming to control the intermolecular energy flow and the reaction course by the chemical bond and vibrational mode selections. There are three typical experimental methods to prepare the molecular vibrational states, such as photoabsorption [1–3], high-temperature heating [6–9], and low-energy electron impact [10–12]. The vibrational mode-selective excitations can be realized by tuning the photon wavelength in the photoabsorption, while the vibrational states prepared by high-temperature heating generally comply with a Boltzmann distribution. The electron impact is a highly efficient method of vibrational excitation, in particular, remarkably benefiting from the larger collision cross sections of the low-energy electrons [10–12]. This vibrational excitation efficiency could be further enhanced, if an electron-molecule resonant state [13], i.e., a molecular transient negative ion (TNI), is experienced in the inelastic collisions with the low-energy electrons. Meanwhile, only specific molecular vibrational modes are selected in the electron-impact resonant excitations, owing to the symmetry matching requirement between the vibrational state and the electronically resonant state [11].

For example, the electron-impact resonant excitations of molecular carbon dioxide (CO_2) have been extensively investigated [10–12,14–17]. Around the TNI resonant state $^2\Pi_u$ of CO_2^-, the vibrational excitations of the symmetric-stretching $\nu_1(\sigma_g^+)$ and the odd-quanta bending $\nu_2(\pi_u)$, rather than the asymmetric-stretching $\nu_3(\sigma_u^+)$, of CO_2 are permitted [11]; meanwhile, dissociative electron attachment (DEA), $e^- + CO_2(X^1\Sigma_g^+) \rightarrow CO_2^-(^2\Pi_u) \rightarrow CO(X^1\Sigma^+) + O^-(^2P)$, is a competitive pathway [6,7,16–21]. For the cold target $CO_2(X^1\Sigma_g^+)$ at its rovibrationally ground state ($\nu = 0$, $j = 0$), the energy threshold (E_{th}) of this DEA process is about 3.988 eV [21]. If the target molecules are in the vibrationally excited states, the dissociation threshold is lowered and the DEA cross section should increase dramatically, e.g., as observed for molecular H_2 [8]. The electron scattering cross sections of the vibrationally excited CO_2 were found to increase by 30% [9,22] or more [23] around the $^2\Pi_u$ state, but there were significant divergences in the previous DEA studies of the heated [6,7,21] and electron-impact excited [10] targets. The threshold was found to shift gradually toward the lower energies as the heating temperature of the gas sample CO_2 increased [6,7,21]; in contrast, this shift was not observed in the electron-impact DEA experiments by using the double electron beams [10]. A succeeding theoretical study predicted the threshold shifts not only for the ν_1-mode but also for the ν_3-mode excitations, and the vibrational excitations of CO_2 also resulted in some intensities and peaklike structures of the O^- production efficiency curve below 4 eV, assuming that the coproduct CO was populated at the vibrationally ground state ($\nu_{CO} = 0$) [22].

Since the DEA and the other electron-induced processes of CO_2 play important roles in planetary atmospheres [24–26], a lot of efforts have been made to explore their dynamics details. However, to date, it is still a challenge to elaborate the DEA dynamics of the vibrationally excited CO_2. Experimentally, a sufficiently high density of excited CO_2 molecules is required for DEA measurements. Moreover, dependent on the excitation methods used, CO_2 molecules may be found in a number of different vibrational states and/or combinations of vibrational states. In the current theoretical model, the DEA is a "half-collision" process, thus the angular distribution of the fragment yield is primarily determined by the resonant-state symmetry of the TNI [13]. It is still unknown whether the target's vibrational states influence the fragmentation kinetics of DEA. Furthermore, most of the theoretical reports on the DEA processes of the molecular vibrational states only concerned simple diatomic molecules [27–29] and are unavailable for polyatomic molecules. Here we report an observation of the

*Corresponding author: sxtian@ustc.edu.cn

DEA to the vibrationally excited CO_2, and gain insight into the complicated dynamics, by recording the O^- momentum images.

II. EXPERIMENTAL METHOD

In our high-resolution anion velocity map imaging apparatus [30], a trochoidal electron monochromator is combined with the ion velocity map imaging technique, leading to anion momentum images with molecular rovibrational-state resolution [30]. Briefly, within a crossed-beam arrangement, the monochromatized pulsed electrons are guided to the reaction region with a homogenous magnetic field (70 G) which is produced with a pair of Helmholtz coils; then the anionic yields are pushed out, accelerated, and flown through the velocity map imaging lens system. In the flight of a given type of anions, different kinetic energies of these anions received in the dissociation result in concentric Newton spheres with different radii. The accelerated anions are detected with a set of multichannel plates plus a phosphor screen. The time-sliced image, i.e., the central slice of the Newton sphere(s), is recorded with a CCD camera mounted behind the phosphor screen and by applying a short high-voltage pulse on the rear multichannel plate. This pulse is also used as the mass gate to selectively detect the anionic yields.

In contrast to the double-electron-beam experiment [10], here we employ the single pulsed electron beam. On the basis of previous work [30], the energy spread of the pulsed incident electrons is further optimized to $\sim$100 meV. The most distinct difference with respect to the previous work is that we use a 400-ns width of the pulsed electrons. When the electron energy is lower than E_{th} (3.988 eV), the front part of this long electron pulse is responsible for the CO_2 vibrational excitations and the residual part is left for the subsequent DEA reaction. The high-purity sample CO_2 is introduced into the reaction region with the heated (335 K) nozzle (300-μm aperture), and the background pressure in the reaction chamber is 1×10^{-6} torr. Two experimental modes, i.e., time-of-flight and time-sliced imaging [30], are operated to record the production efficiency curve and the momentum images of the O^- yield, respectively.

III. RESULTS AND DISCUSSION

As shown in Fig. 1, the present production efficiency curve is compared with those reported previously [20,21]. The profiles of the latter [20,21] are similar to what we obtained with the lower-energy resolution (the pulsed electron energy spread of 145 meV), the shorter electron pulse (200-ns width), and the cold molecule beam [30]. Below the E_{th} value of 3.988 eV (denoted with a vertical dashed line), the present curve (red) exhibits strong intensities and six peaks, and these O^- anions are definitely produced in the DEA to the vibrationally excited CO_2. Three weak peaks are at 2.95(**1′**), 3.05(**2′**), and 3.16 eV(**3′**), and three strong ones are at 3.34(**1**), 3.59(**2**), and 3.83 eV(**3**). Below 3.22 eV, the inelastic cross section of CO_2 showed the structureless shoulder which was irrelevant to the $^2\Pi_u$ resonant state [17], thus peaks **1′**–**3′** should be attributed to the nonresonant excitations and will not be discussed further in this paper. After the electron

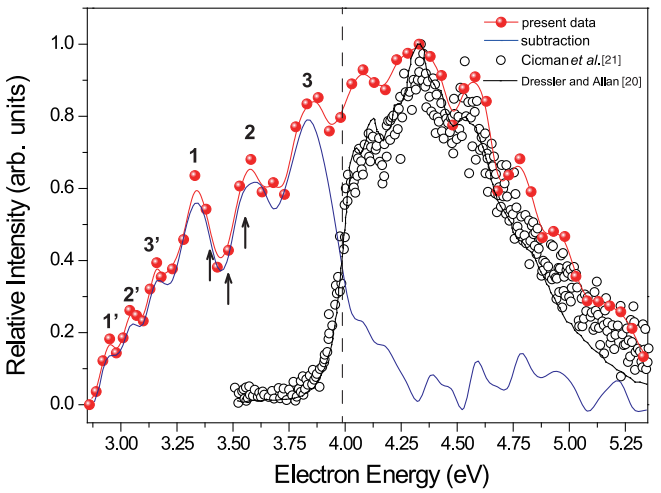

FIG. 1. O^- production efficiency curves obtained for the DEA to CO_2 at the different vibrational states (solid circles and curve in red, this paper) and the DEA to the cold target CO_2 (black curve, Dressler and Allan [20]; empty circles, the result from Cicman *et al.* [21]) after the renormalizations. The blue curve is the anion production subtracting the data in [21] from the present data. The vertical dashed line represents the threshold of the latter process, and the arrows denote the energy positions to record the O^- momentum images. Assignments of peaks **1′**–**3′** and **1**–**3** can found in the text.

collisions at 4.2 eV, only one weak broad peak around 1.0 eV was observed in the subsequent DEA [10]. In the present paper, the vibrational excitation and the subsequent DEA process are accomplished within one electron pulse where the electrons have the same kinetic energy. In the higher-energy part of the present curve, the peaklike bumps become more significant than those observed previously [20,21,30]. The difference curve (blue) is plotted by subtracting the cold-sample contribution [21] from the present curve (red), indicating the remarkable contributions of the vibrationally excited sample at the attachment energies below the E_{th} values. When the electron energy is higher than the E_{th} value, most electrons will be involved in the DEA process, thus the vibrational excitations can be ignored. Below the E_{th} value, two sets of peaks show somehow equivalent intervals, i.e., about 0.10 eV among peaks **1′**–**3′** and 0.25 eV among peaks **1**–**3**. At a given electron energy, the vibrationally excited states of ν_1 and ν_2 modes with various quanta, as well as their different combinations, can be populated [10–12,14–17], and each of them could enhance the DEA cross sections. Therefore, much caution should be practiced for assignments to these peaks.

To diminish the possible interferences from the contributions of the high (above E_{th}) and low (weak peaks **1′**–**3′**) electron energies, we recorded the O^- momentum images at 3.38, 3.48, and 3.58 eV (denoted with the arrows in Fig. 1). These images are shown in Figs. 2(a)–2(c), where the ion intensity in each image is normalized independently, the weighted volume in one bin is equivalent, and the image size is scaled with the pixel numbers. In general, the backward (upper) distributions show higher intensities than those of the forward (down) distributions, the anisotropic angular distribution is superimposed on the strong background in each image, and

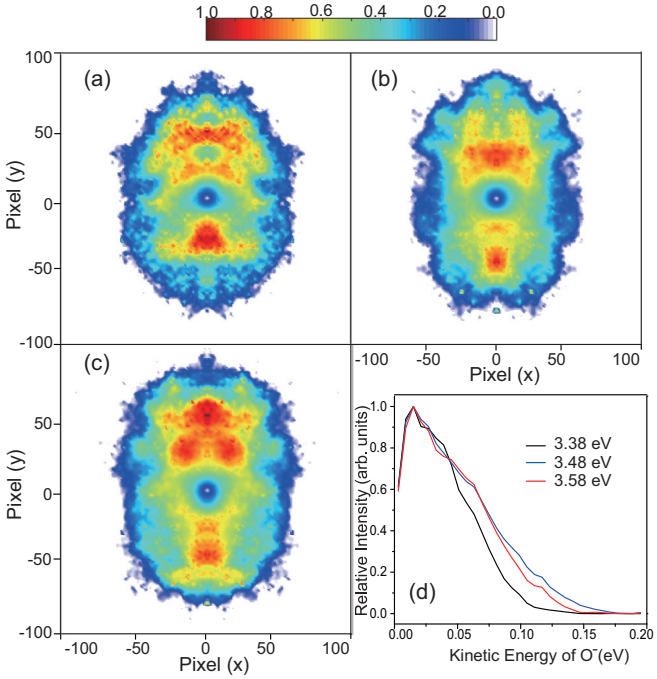

FIG. 2. O^- momentum images at 3.38 (a), 3.48 (b), and 3.58 eV (c). The electron incident direction (along the y axis) is from top (backward) to bottom (forward) and through the image center. The O^- kinetic-energy distributions (d) are obtained from the images (a–c) after the intensity renormalizations.

the anisotropy varies with the electron energy. The O^- kinetic energy (E_k) can be derived with the distance of the signal position from the image center. The $E_k(O^-)$ distributions of the full-angle signals are plotted in Fig. 2(d) and show less than 0.20 eV for the most O^- anions.

Within the principles of energy and momentum conservations, the $E_k(O^-)$ is determined with

$$E_{\mathrm{k}}(\mathrm{O}^-) = \frac{m_{\mathrm{CO}}}{M_{\mathrm{CO_2}}}\left(E_e - E^{v}_{\mathrm{th}} - E_{\mathrm{int}}\right) \qquad (1)$$

where m and M are the masses of CO and CO_2; E_e, $E^{v}{}_{\mathrm{th}}$, and E_{int} are the electron attachment energy, the dissociation threshold of CO_2, at the vibrational state v, and the internal energy of $CO(X^1\Sigma^+)$ at the rovibrational states (v, j), respectively. According to the vibrational energies [31] and the $^2\Pi_u$-resonant excitation cross sections of CO_2 [10–12,14–17], in Fig. 3 we make the assignments for the E_k distributions of the backward (scattering angle $\theta = -165^\circ$ to 165°) O^- anions. As shown in Fig. 85 of [17], two series of the vibrational progressions, $(n, 0, 0)$ and $(n, 1, 0)$ of CO_2 (ν_1, ν_2, ν_3), were clearly identified in the electron-impact exitations at 3.5 eV; furthermore, there were the larger cross sections for $n = 3, 4, 5$, and 6 in the electron energy-loss range of 0.5–1.0 eV. The bond bending motion $\nu_2 = 1$ is disfavored in principle due to the symmetry limitation [11], but can be activated in the experiments, because the CO_2 structure is slightly bent in thermostatistics. The energy (about 0.065 eV) of the mode ν_2 above its ground state $\nu_2 = 0$ is much lower than those of the other modes, thus the lowest vibrational states of ν_2 will be populated even at room temperature [23].

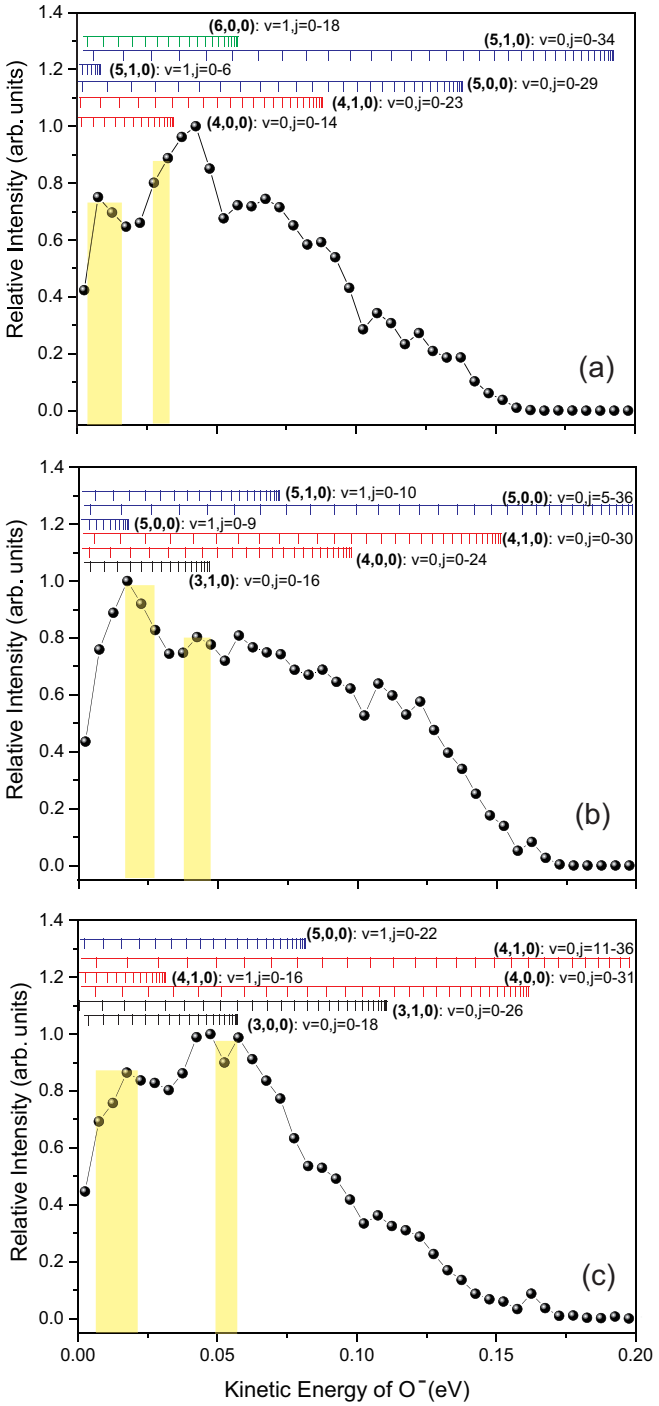

FIG. 3. Spectral assignments of the kinetic-energy distributions of the backward scattering O^- anions at the electron energies of 3.38 (a), 3.48 (b), and 3.58 eV (c), by using the vibrational states, (ν_1, ν_2, ν_3) noted with thick numbers, of CO_2 and the rovibrational (v, j) states of the CO product. The vertical bars colored in yellow represent the O^- anions with the selected kinetic energies for plotting the angular distributions.

The sample heating in this paper leads to higher populations at $\nu_2 = 1$. Once the vibrational state (E^{ν} denotes its energy) of CO_2 is confirmed, $E^{\nu}{}_{th}$ can be obtained as the difference between E_{th} and E^{ν}. According to Eq. (1), we

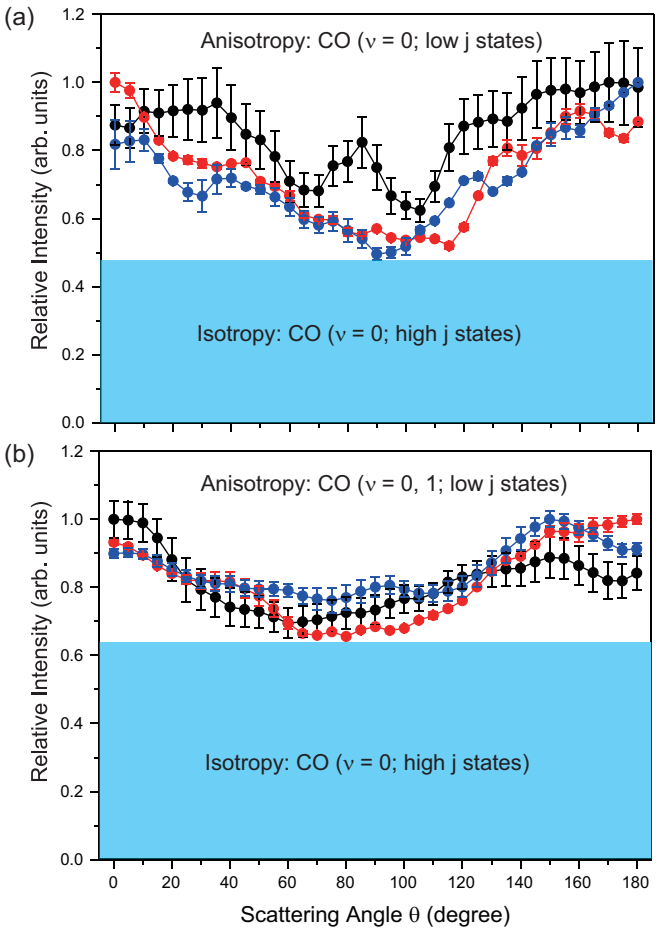

FIG. 4. Angular distributions of the O^- ions with the selected kinetic energies. Black circles, $E_k(O^-) = 0.026 - 0.034$ eV (a) and $0.003 - 0.014$ eV (b) at the electron energy of 3.38 eV; blue circles, $E_k(O^-) = 0.039 - 0.047$eV (a) and $0.015 - 0.027$ eV (b) at the electron energy of 3.48 eV; red circles, $E_k(O^-) = 0.051 - 0.057$ eV (a) and $0.005 - 0.021$ eV (b) at the electron energy of 3.58 eV. In each panel, the bottom colored in blue denotes the isotropic background, while the upper shows the anisotropic distributions.

further derive the $E_{\rm int}$ values, then make assignments with the corresponding rovibratioanl states of CO in Fig. 3. Here the contributions of the higher vibrational states of $n \geqslant 7$ are excluded, due to the dramatic decrease of the excitation cross section with the increase of the electron energy loss [17]. The CO products are apt to be populated at the vibrationally ground ($\nu_{\rm CO} = 0$) and the first excited ($\nu_{\rm CO} = 1$) states but at various rotational states. One also can find some correlations between the spectral heads of the $(n, 0, 0)/(n, 1, 0)$ series and the peaks or shoulders of the profile in Fig. 3, indicating the individual contribution of each CO_2 vibrational state to the DEA processes.

In Fig. 4, we further plot the O^- angular distributions with the selected $E_k(O^-)$ ranges shown with the yellow vertical bars in Fig. 3. These $E_k(O^-)$ values correspond to the significantly anisotropic distributions observed in the images of Figs. 2(a)–2(c). In general, the angular distributions of the high-$E_k(0.026 - 0.057\,\text{eV})O^-$ anions are more anisotropic [Fig. 4(a)] than those of the slow-$E_k(0.003 - 0.027\text{eV})$ ones [Fig. 4(b)], but both of them are superimposed on the isotropic distributions. In whole scattering angle range, the intensity variations of the anisotropic component are less than 53% [Fig. 4(a)] or 47% [Fig. 4(b)] of the respective total. If the CO moiety in CO_2^- receives a large torque by the bond bending, the CO products are apt to be populated at the highly rotational states, otherwise the slowly rotating CO will be produced. As shown in Fig. 3(a), the slowly rotating CO fragments in the selected $E_k(O^-)$ ranges (marked with the yellow bars) may be produced via $e^- + CO_2(5, 1, 0) \rightarrow CO(\nu = 1, j = 0 - 6) + O^-$ and $e^- + CO_2(4, 0, 0) \rightarrow CO(\nu = 0, j = 3 - 6) + O^-$, and exhibit the anisotropic angular distribution at 3.38 eV (black circles) shown in Fig. 4(b). The fragment rotations can be sufficiently developed if the predissociative parent molecule survives in dozens of molecular rotation periods, leading to the nearly isotropic angular distributions of the highly rotating fragments [32]. Therefore, with reference to Fig. 3(a), the isotropic background of the angular distribution (black circles) at 3.38 eV in Fig. 4(a) should be attributed to the highly rotating CO anions ($\nu = 0$) at $j = 19$ and 20 via the DEA to $CO_2(4, 1, 0)$ and those at $j = 25$ and 26 via the DEA to $CO_2(5, 0, 0)$. Similarly, the isotropic background at 3.38 eV in Fig. 4(b) arises from those at $j = 22$ and 23 via the DEA to $CO_2(4, 1, 0)$ and those at $j = 27-29$ via the DEA to $CO_2(5, 0, 0)$. Similar scenarios can be found at the other electron energies.

As shown in Fig. 4, the isotropy-to-anisotropy ratios depend on the $E_k(O^-)$ values, but the isotropic feature is basically predominant. Thereby, the origins of the highly rotating CO, i.e., some specific vibrational states of CO_2 as assigned in Fig. 3 and discussed above, can be used to asssign peaks **1**, **2**, and **3** observed in Fig. 1. With reference to the vibrational energies of CO_2 [31] and on the basis of the analyses for Figs. 3 and 4, we can extrapolate that the predominant contributions are (5, 1, 0) and (6, 1, 0) states to **1**, (4, 0, 0) and (5, 0, 0) states to **2**, and (2, 1, 0) and (3, 1, 0) states to **3**. Obviously, the other vibrational states of CO_2 are also important, in particular, for the anisotropic angular distributions of the fragments.

IV. CONCLUSION

In summary, we report an observation of the molecular vibrational-state effects on the DEA process of CO_2. Although it is still a challenge to describe this process precisely in theory, we demonstrate an experimental evidence about the enhancement of chemical reaction activity by electron impact. The vibrational resonant excitation in molecule-electron collision, in particular its vibrational mode selectivity, is potentially applicable in the manipulations of chemical reaction. In our group, the double-electron-beam "pump-probe" technique is being developed and its application for the DEA process will be combined with ion velocity imaging method.

ACKNOWLEDGMENTS

This work is supported by National Natural Science Foundation of China (Grants No. 21727804 and No. 21625301).

[1] F. F. Crim, Proc. Natl. Acad. Sci. USA **105**, 12654 (2008).
[2] W. Zhang, H. Kawamata, and K. Liu, Science **325**, 303 (2009).
[3] T. Wang, J. Chen, T. Yang, C. Xiao, Z. Sun, L. Huang, D. Dai, X. Yang, and D. H. Zhang, Science **342**, 1499 (2013).
[4] J. C. Owrutsky, D. Raftery, and R. M. Hochstrasser, Annu. Rev. Phys. Chem. **45**, 519 (1994).
[5] L. Chen, J. A. Lau, D. Schwarzer, J. Meyer, V. B. Verma, and A. M. Wodtke, Science **363**, 158 (2019).
[6] D. Spence and C. J. Schulz, Phys. Rev. **188**, 280 (1969).
[7] P. J. Chantry, J. Chem. Phys. **57**, 3180 (1972).
[8] M. Allan and S. F. Wong, Phys. Rev. Lett. **41**, 1791 (1978).
[9] S. J. Buckman, M. T. Elford, and D. S. Newman, J. Phys. B **20**, 5175 (1987).
[10] S. K. Srivastava and O. J. Orient, Phys. Rev. A **27**, 1209 (1983).
[11] D. C. Cartwright and S. Trajmar, J. Phys. B **29**, 1549 (1996).
[12] H. Kato, M. Ohkawa, M. Hoshino, L. Campbell, M. J. Brunger, and H. Tanaka, J. Phys.: Conf. Ser. **204**, 012002 (2010).
[13] T. F. O'Malley and H. S. Taylor, Phys. Rev. **176**, 207 (1968).
[14] V. Laporta, J. Tennyson, and R. Celiberto, Plasma Sour. Sci. Tech. **25**, 06LT02 (2016).
[15] C. W. McCurdy, W. A. Isaacs, H.-D. Meyer, and T. N. Rescigno, Phys. Rev. A **67**, 042708 (2003).
[16] C. F. Wong and J. C. Light, Phys. Rev. A **33**, 954 (1986).
[17] M. Allan, J. Electron Spectrosc. Relat. Phenom. **48**, 219 (1989).
[18] M. J. W. Boness and G. J. Schulz, Phys. Rev. Lett. **21**, 1031 (1968).
[19] R. Abouaf, R. Paineau, and F. Fiquet-Fayard, J. Phys. B **9**, 303 (1976).
[20] R. Dressler and M. Allan, Chem. Phys. **92**, 449 (1985).
[21] P. Cicman, G. Senn, G. Denifl, D. Muigg, J. D. Skalny, P. Lukac, A. Stamatovic, and T. D. Märk, Czech J. Phys. **48**, 1135 (1998).
[22] J. Ferch, C. Masche, W. Raith, and L. Wiemann, Phys. Rev. A **40**, 5407 (1989).
[23] W. M. Johnstone, M. J. Brunger, and W. R. Newell, J. Phys. B **32**, 5779 (1999).
[24] L. Campbell, M. J. Brunger, and T. N. Rescigno, J. Geophys. Res. **113**, E08008 (2008).
[25] L. Campbell, M. Allan, and M. J. Brunger, J. Geophys. Res. **116**, A09321 (2011).
[26] X.-D. Wang, X.-F. Gao, C.-J. Xuan, and S. X. Tian, Nat. Chem. **8**, 258 (2016).
[27] J. Horáček, M. Čížek, K. Houfek, P. Kolorenč, and W. Domcke, Phys. Rev. A **70**, 052712 (2004).
[28] P. Kolorenč and J. Horáček, Phys. Rev. A **74**, 062703 (2006).
[29] V. Laporta, R. Celiberto, and J. Tennyson, Phys. Rev. A **91**, 012701 (2015).
[30] X.-D. Wang, X.-F. Gao, H. Li, and S. X. Tian (unpublished).
[31] L. S. Rothman and L. D. Young, J. Quant. Spectrosc. Radiat. Transfer **25**, 505 (1981).
[32] R. N. Zare and D. R. Herschbach, Proc. IEEE **51**, 173 (1963).